

Strong Optical Absorption in AgBiS₂ Nanocrystals enabled by Cation Disorder Engineering for Highly Efficient Extremely Thin Absorber Solar Cells

Yongjie Wang^{1†}, Seán R. Kavanagh^{2,3†}, Ignasi Burgués-Ceballos¹, Aron Walsh^{3,4}, David Scanlon^{2,5}, Gerasimos Konstantatos^{1,6*}

¹ICFO-Institut de Ciències Fotoniques, The Barcelona Institute of Science and Technology, Castelldefels, 08860 Barcelona, Spain.

²Thomas Young Centre and Department of Chemistry, University College London, London WC1H 0AJ, U.K.

³Thomas Young Centre and Department of Materials, Imperial College London, London SW7 2AZ, U.K.;

⁴Department of Materials Science and Engineering, Yonsei University, Seoul 03722, Republic of Korea.

⁵Diamond Light Source Ltd., Diamond House, Harwell Science and Innovation Campus, Didcot, Oxfordshire OX11 0DE, UK

⁶ICREA-Institució Catalana de Recerca i Estudis Avançats, Lluís Companys 23, 08010 Barcelona, Spain.

[†]These authors contributed equally to this work.

*e-mail: Gerasimos.Konstantatos@icfo.eu

Strong optical absorption of a semiconductor is a highly desirable property for a material to be considered in optoelectronic and photovoltaic applications. Strong light absorbers can enable ultrathin solar cells and photodetectors that in turn lead to significant reductions in cost, weight and manufacturing throughput as well as improve quantum efficiency and performance. The optimal thickness of a semiconductor absorber is primarily determined by its absorption coefficient. To date, this parameter has been considered as a fundamental material property and efforts to realize thinner photovoltaics have relied on light-trapping structures that add complexity and cost. Here, we demonstrate that by engineering cation disorder homogeneity in a ternary chalcogenide semiconductor leads to significant absorption increase due to enhancement of the optical transition matrix elements. We show that cation disorder engineered AgBiS₂ colloidal nanocrystals offer an absorption coefficient that is higher than any other photovoltaic material used to date, enabling highly efficient extremely thin absorber (ETA) photovoltaic devices. Leveraging this high absorption and by further optimization of the electron and hole blocking layers we report solution-processed, environmentally-friendly, 30nm thick ETA solar cells with short circuit current density of 27 mA·cm⁻², a

record power conversion efficiency of 9.17% (8.85% certified) and high stability under ambient conditions.

High-performance, lightweight solar cells featuring low cost and environmental friendliness have been a long-sought target in the photovoltaic field. Ultrathin solar cells can reduce material consumption and manufacturing demands, directly lowering the cost. Owing to an absorber thickness that is orders of magnitude lower than conventional solar cells, ultrathin solar cells further allow for flexible and light-weight form factors suited for building- or wearable- integrated photovoltaics. A thinner absorber layer also improves charge carrier collection and reduces bulk recombination, which are particularly prevalent in nanocrystalline solution-processed semiconductors^{1,2}, thus improving performance provided strong light absorption. Furthermore, high absorption in small absorber volumes allows for operating the device at high photo-generated carrier densities, a physical regime which maximizes the open-circuit voltage (V_{oc}) and permits advanced high-efficiency concepts such as hot-carrier solar cells³.

Currently, high performance ultrathin solar cells are mainly realized via different light-trapping strategies, which are employed to compensate for the short circuit current drop due to incomplete absorption in the ultrathin absorbing layer^{4,5}. The use of optical architectures, however, increases non-radiative recombination^{4,6} and complicates the manufacturing process, introducing additional obstacles toward low-cost high-efficiency devices.

Typically, the absorption coefficient of a material determines the required thickness for optimal light harvesting under photovoltaic operation. The absorption coefficient of a semiconductor has been considered as a fundamental parameter of the material, with efforts to enhance light absorption in ultrathin absorbers relying on optical means^{4,5}. We instead took the view - motivated by the fundamental relationship between atomic geometry, electronic structure and

optical absorption - that the absorption coefficient of a semiconductor can be tuned by engineering the atomistic material structure.

Cation disorder is a widely observed phenomenon in multinary materials, referring to the deviation of atomic positions in the cationic sublattice from an ordered crystalline arrangement. This phenomenon significantly impacts the optoelectronic properties of semiconductors⁷⁻⁹ and has traditionally been considered an undesirable (and often unavoidable) effect, due to its entropically-driven nature^{7,8,10,11}. Herein, we leverage the modulation of cation disorder homogeneity in multinary semiconductors as a pathway to enhancing optical transition matrix elements, in order to achieve improved absorption coefficient and photovoltaic device efficiency.

Cation disorder homogeneity and absorption behaviour

In this work, we focus on ternary AgBiS₂ nanocrystals (NCs), a solution-processed nanomaterial comprising environmentally-friendly elements^{12,13} with reported efficiencies exceeding 6% in thin-film solar cells^{1,14}. The cation distribution around Ag sites in AgBiS₂ nanocrystals has shown evidence for non-random Ag-Ag correlation¹⁵, indicating the presence of inhomogeneous cation disorder (i.e. cation segregation with local Ag-rich and Bi-rich regions), likely due to growth kinetics during synthesis and surface ligand interactions¹⁶⁻¹⁸.

An illustration of inhomogeneous cation disorder within AgBiS₂ NCs is shown in Fig. 1a. The valence band maximum (VBM) of AgBiS₂ primarily derives from Ag *d* and S *p* states, while the conduction band minimum (CBM) arises from Bi *p* and S *p* interactions^{19,20} (Fig. 1b). A clear spatial separation of the Ag-derived VBM and Bi-derived CBM for the cation-segregated configuration can be observed in the local electronic density of states (LDOS), shown in Fig. 1c. In contrast, under homogeneous cation disorder, we predict a VBM and CBM delocalized

over the entire material (Fig. 1d), with the correlation between cation distribution and spatial (de)localization of the band extrema further demonstrated by Fig. 1e.

The theoretically simulated absorption spectra of AgBiS₂ for both inhomogeneous and homogenous cation disorder are provided in Fig. 2a. As expected, we find a substantially increased refractive index n and transition dipole matrix element (Supplementary Fig. 1), thus enhanced optical absorption upon homogenizing disorder.

To experimentally tune cationic disorder, we first assessed the thermodynamics of atomic reordering, in particular the formation energy difference needed to induce disorder. Density Functional Theory (DFT) was employed to calculate the inter-site cation exchange energy. Under the highest level of theory employed for phase energetics (hybrid DFT including spin-orbit coupling effects), the bulk order-disorder enthalpy difference is calculated as 17.4 meV/atom, indicating the accessibility of cation site-swapping in AgBiS₂ under mild annealing conditions. The mechanism behind cation inter-site exchange is likely defect-mediated ionic migration. Indeed, cation mobility aided by Ag vacancies and bond anharmonicity has been demonstrated in AgBiS₂ nanocrystals^{21–23}. Considering the low inter-site cation exchange energy in AgBiS₂, we sought to anneal AgBiS₂ NCs under low-temperature conditions to facilitate cation inter-site exchange and thus an entropically-driven transition to homogenous cation distribution. Fig. 2b plots the absorption coefficient of our NC films upon annealing under different temperatures. Comparing Fig. 2a and 2b, the simulated absorption spectrum for cation segregation configurations (inhomogeneous disorder) matches well with the as-prepared AgBiS₂ NC film, both exhibiting Urbach tailing at longer wavelengths, which is pernicious for photovoltaic devices^{24,25}. However, in the homogenous cation-disordered structure, the simulated absorption coefficient is much higher than the cation-segregated case, with reduced bandtailing, manifesting favourable properties for optoelectronic applications²⁶. As shown in Fig. 2b, the absorption coefficient of AgBiS₂ NCs films is enhanced by up to a factor of two

1 after annealing, alongside reduced Urbach energy from 173.2 meV to 25.7 meV
2 (Supplementary Fig. 2), as predicted by *ab initio* calculations. Furthermore, this enhanced
3 absorption is stable in ambient atmosphere, as spontaneous cation segregation is
4 thermodynamically and entropically unfavourable (Supplementary Fig. 3). With this low-
5 energy and scalable annealing process, we produce a semiconducting material that exhibits an
6 absorption coefficient 5-10 times greater than any other material currently used in photovoltaic
7 technology^{4,27-31}, across a wide spectral range from 400 – 1000 nm (Fig. 2c).

8 With the high absorption coefficient of our films, an ultrathin layer of AgBiS₂ NCs would be
9 sufficient to absorb most of the light in the visible range. In order to assess the potential of our
10 strongly-absorbing NC films, we calculate the maximum achievable short-circuit current
11 density J_{sc} using the transfer matrix method^{32,33}, assuming 100% internal quantum efficiency
12 (Supplementary Fig. 4). Fig. 2d plots the maximum J_{sc} as a function of the active layer
13 thickness for different annealing temperatures, corresponding to varying degrees of cation
14 disorder homogeneity. Upon increased annealing temperature, we witness an increase in J_{sc}
15 reached at low active layer thicknesses ($t < 200$ nm). We predict a maximum J_{sc} of ~28 (32)
16 mA·cm⁻² for AgBiS₂ NCs films annealed at 115°C (150°C), with thicknesses of only ~30 nm.
17 Furthermore, the Spectroscopic Limited Maximum Efficiency (SLME) was calculated
18 assuming only radiative recombination in devices³⁴. As shown in Fig. 2e, a high photovoltaic
19 efficiency up to 26% was predicted for a 30 nm absorber layer, indicating the performance
20 potential of ultrathin solar cells based on AgBiS₂ NC films. Furthermore, with the thickness
21 reduction of AgBiS₂ absorber from 500 nm (common photovoltaic thickness) to 30 nm, we
22 estimate a ~50% cost reduction over the full PV device cost (Supplementary Fig.5 and
23 Supplementary Note 1).

Cation configuration transition

To further verify the proposed cation homogenization as the underlying mechanism responsible for the optical absorption enhancement in AgBiS₂ NC films, film thicknesses were first measured to exclude nanocrystal densification as the dominant factor. Negligible thickness changes were observed between the as-prepared and 115 °C annealed samples (Supplementary Fig. 6), with only a slight decrease for the 150 °C annealed films, contributing to a very small (~8%) absorption enhancement for this sample. These film thickness measurements demonstrate that densification effect is not the dominant factor in the absorption enhancement of these materials. Furthermore, we used X-Ray Diffraction (XRD) and Transmission Electron Microscopy (TEM) to probe the changes in crystal structure due to cation disorder homogenization upon annealing. Interestingly, while XRD analysis suggested increased crystallite size (from 4.2 nm to 6.2 nm) upon annealing at 115°C, High Resolution Transmission Electron Microscopy (HRTEM) showed no measurable size differences in these samples (Supplementary Fig. 7). The sharpening of XRD peaks despite negligible NC growth indicates an improved crystallinity due to atomic rearrangements within the nanocrystals. Further increasing the annealing temperature to 150°C and 200°C causes NCs to fuse to larger crystals (28 nm and 47 nm, Supplementary Fig. 7). Point defects are observable from HRTEM after high temperature annealing, which could be harmful for optoelectronic applications³⁵ (Supplementary Fig. 8). In addition to peak narrowing in XRD patterns, the peak positions were also found to shift to higher angles upon annealing (Fig. 3a). To deconvolute the effect of crystal size and cation arrangement, and explain the apparent changes in crystallinity, we calculated the expected XRD patterns for homogeneously disordered cubic AgBiS₂ (space group $Fm\bar{3}m$, Supplementary Fig. 9), with crystal size as the only variable parameter (Supplementary Fig. 10). The full width half maximum (FWHM) of all peaks sharpens with crystal growth, while the peak positions remain essentially the same, as expected. However,

transitioning from cation-segregated configurations to homogeneous cation disorder, while fixing the crystallite size, the simulated XRD patterns of AgBiS₂ show distinct peak shifts to higher angles as well as peak narrowing (Fig. 3b), matching the experimental observations of improved crystallinity upon annealing. The XRD peak shifts primarily originate from the shortening of Ag-S bond lengths, while peak narrowing occurs due to narrowing of the bond length distributions and reduction of octahedral distortion, upon homogenization of the cation distribution (Supplementary Fig. 11). This phenomenon was further confirmed with HRTEM measurements, as shown in Fig. 3c and d, with integrated line profiles of the {200}-plane showing a slight shrinkage after annealing, further confirming the transition from cation segregation to homogeneous disorder.

Considering the difference in local bonding environments for different cation configurations, changes in Madelung potential were expected³⁶. We calculate the average Madelung potential at Bi sites as 3.29 V and 4.66 V for segregated and homogeneous cation configurations, respectively, using Bader atomic charges. A greater Madelung potential suggests a decrease in XPS binding energy, upon transitioning from inhomogeneous to homogeneous cation disorder^{36,37}. As shown in Fig. 3e, the Bi 5*d* peaks in the simulated XPS spectra are noticeably shifted to lower binding energies for homogeneous cation disorder, as compared to cation-segregated configurations. Likewise, the annealed AgBiS₂ NCs show a small but significant chemical shift to lower energy, compared with as-prepared samples (Fig. 3f and g), in agreement with our proposition of cation homogenization upon annealing.

Ultrathin AgBiS₂ NC solar cells

Having developed a material with such strong optical absorption, we next sought to produce highly efficient ultrathin solution-processed solar cells with these nanocrystals. Solar cells were fabricated with an architecture of Glass/ITO/SnO₂/AgBiS₂/HTL/MoO₃/Ag, as shown in Fig.

4a. Cross-sectional Transmission Electron Microscopy (TEM) confirms the ultrathin nature of the device layers (Fig. 4b). We first used PTB7 as an electron blocking layer, in accordance with previous studies^{1,14}. The devices showed an average power conversion efficiency (PCE) of $6.4 \pm 0.6\%$, with a champion device reaching PCE of 7.6% (Table 1) – higher than the previously reported record performance of 6.3%^{1,14,38–40}. Atomic Force Microscopy (AFM) revealed a surface roughness of 0.6 nm for a 4 nm PTB7 film (Supplementary Fig. 12), which undermines the performance of the cells by introducing interface recombination⁴¹. We sought to replace PTB7 with an alternative electron-blocking layer with improved morphological characteristics. We found that PTAA yielded improved uniformity (RMS roughness of 0.4 nm), a prerequisite for suppressing current leakage and interface recombination. In order to further assess the superiority of PTAA, transient photocurrent and photo-voltage were measured under one-Sun light bias (Supplementary Fig. 13). Devices with PTAA showed a faster photocurrent decay and longer carrier lifetime than that with PTB7 as the HTL, which indicates improved charge extraction and reduced interface recombination. As a result, replacing PTB7 with PTAA leads to significant improvement in V_{oc} and fill factor (FF) (Supplementary Fig. 12), and results in a ~20% increase in power conversion efficiency to $8.7 \pm 0.3\%$, with a best device reaching 9.17% (Fig. 4c and d). One of our champion devices was sent to an accredited PV calibration laboratory (Newport, USA), which certified a PCE of 8.85% under AM1.5G full sun illumination, with negligible hysteresis (Fig. 4e, Supplementary Fig. 14). The measured J_{sc} of $27 \text{ mA} \cdot \text{cm}^{-2}$ was further confirmed by the external quantum efficiency (EQE) spectrum, which gives a value of $26.5 \text{ mA} \cdot \text{cm}^{-2}$ (Fig. 4f). In addition, the measured EQE spectrum matched well with the TMM predicted EQE, indicating a near-unity internal quantum efficiency (IQE). However, unannealed devices showed not only lower absorption (i.e. predicted EQE) in near infrared region, but also a lower IQE (Fig. 4f) and larger V_{oc} deficit, which is ascribed to slower charge extraction, Urbach band tailing and higher trap density (Supplementary Fig. 15). Higher

temperature annealing leads to significantly lower performance, which is consistent with the defects forming from uncontrolled nanocrystal fusing (Supplementary Fig. 8 and Fig. 16). Analysing the absorption loss of our record performance ultrathin devices, a large part of the incident light ($\sim 10 \text{ mA}\cdot\text{cm}^{-2}$) was reflected (Supplementary Fig. 17) and further improvement of device performance is expected by introducing an antireflection layer.

On the other hand, thicker (200 nm) devices are also fabricated for direct comparison with ultrathin devices and, as expected, a low J_{sc} ($\sim 15 \text{ mA}\cdot\text{cm}^{-2}$) was obtained (Supplementary Fig. 18). In order to further understand the devices, time-of-flight (ToF) was employed to investigate the charge carrier mobilities in our AgBiS₂ NC films (Supplementary Fig. 19). The hole and electron mobility are calculated to be 1.2×10^{-4} and $5.7 \times 10^{-5} \text{ cm}^2\cdot\text{V}^{-1}\cdot\text{s}^{-1}$, respectively. Combining with the carrier lifetime extracted from TPV measurements, the diffusion length is estimated to be $\sim 25.4 \text{ nm}$, which rationalizes the near-unity IQE in our 30 nm devices and the low performance in 200 nm thick devices. Mid-gap trap density was estimated from TPC/TPV measurements (Supplementary Fig. 15). In our optimal AgBiS₂ NC films, the trap density is $\sim 9 \times 10^{16} \text{ cm}^{-3}$. Although this trap density is four times lower than before annealing ($\sim 4 \times 10^{17} \text{ cm}^{-3}$), efforts are needed to further passivate the trap states for higher V_{oc} and thus, higher efficiency.

In addition to power conversion efficiency, stability is another important figure-of-merit of photovoltaic devices. Therefore, in order to assess the stability of our AgBiS₂ NC solar cells, we first measured their shelf lifetime by storing the un-encapsulated devices in ambient conditions with a temperature of $\sim 25^\circ\text{C}$ and relative humidity of $\sim 30\%$. The device showed a gradual improvement in the first 20 days (Supplementary Fig. 20), which is likely a result of oxidation of MoO_x layer and a better band alignment⁴⁴ (Supplementary Fig. 21). Furthermore, the device retained its original performance after four months' aging. The operational stability was further investigated by subjecting the un-encapsulated device to AM1.5G one sun

illumination in ambient atmosphere with relative humidity ~ 60%. The device performance was measured by applying a forward bias fixed at the maximum power point (MPP). As shown in Fig. 4g, the PCE of the PTB7 device dropped below 2% after 20 minutes illumination, while the PTAA device demonstrated much better operational stability under continuous operation. After 10 hours MPP testing on un-encapsulated cell in ambient conditions, the device retained 85% of its original efficiency. Longer stability at MPP was also recorded with a class AA solar light source, showing ~80% of original performance after 40h test in ambient air (Supplementary Fig. 22). To our knowledge the devices reported herein set a record among low-temperature and solution-processed, non-toxic inorganic solar cells in terms of stability and performance^{45–48}. These results support that AgBiS₂ NCs is extremely promising material for low-cost, efficient, stable and environmentally friendly solar cells.

In conclusion, we have demonstrated that the absorption coefficients of ternary AgBiS₂ NCs can be enhanced via cation disorder homogenization at mild annealing conditions. Ultra-high absorption coefficients were obtained in annealed AgBiS₂ NC films, with a calculated SLME of over 26% for a 30 nm NC film. The transition in cation configuration was further confirmed by the combination of *ab initio* calculations with XRD, HRTEM and XPS measurements. Ultrathin solar cells are fabricated based on ultra-absorbing AgBiS₂ NCs. A high J_{sc} of 27 mA·cm⁻² and a record efficiency up to 9.17% were obtained with an independent certification of 8.85% from Newport. The air stability and photostability was also recorded in high performance devices. Our work not only establishes the potential of ultrathin AgBiS₂ NC solar cells, which are solution-processable and RoHS-compliant, but also demonstrates the importance of atomic configuration engineering in multinary systems.

1 Methods

2 **Density Functional Theory (DFT) simulations.** The AiiDA infrastructure was used to
3 maintain data provenance for all calculations performed in this study⁴⁹. Calculations were
4 performed using Density Functional Theory (DFT) within periodic boundary conditions
5 through the Vienna *Ab Initio* Simulation Package (VASP)^{50–52}. Using the projector-augmented
6 wave method, scalar-relativistic potentials were employed to describe the interaction between
7 core and valence electrons.⁵³ Calculations were carried out using Γ -centred k-point meshes
8 with a reciprocal space sampling of 0.11 \AA^{-1} and a plane-wave kinetic energy cutoff of 300 eV
9 (increased to 450 eV for structural relaxations, to avoid the possibility of Pulay stress). With
10 these parameter choices, the ground-state energies of all known structures in the Ag-Bi-S
11 system were converged to within 1 meV/atom.

12 **Cation Disorder.** To model the effects of varying degrees of cation order/disorder, two
13 approaches were employed. Firstly, to simulate total random cation disorder, a 64-atom
14 supercell for AgBiS₂ in the $Fm\bar{3}m$ rocksalt structure was generated using the special quasi-
15 random structure (SQS) method⁵⁴, in which the cation-cation cluster correlations are optimised
16 to obtain the best approximation to an ideal infinite random distribution for a given supercell.
17 Here, the Alloy Theoretic Automated Toolkit (ATAT)⁵⁵ was used to generate the SQS supercell
18 via Monte-Carlo simulated annealing loops⁵⁶. Eight Monte-Carlo simulations were performed,
19 with the structure giving the best match to the true disordered solid solution chosen for further
20 calculations. This corresponded to an ‘objective function’ of -81.18; considering 2-atom
21 clusters up to 12 \AA separation, 3-atom clusters up to maximum 10 \AA pair separation and 4-
22 atom clusters up to 8 \AA pair separation (using the experimental rocksalt crystal structure)³⁷.
23 The screened hybrid DFT exchange-correlation functional of Heyd, Scuseria and Ernzerhof
24 (HSE06)³⁸ was used to calculate the structural and electronic properties of $Fm\bar{3}m$ (using this
25 SQS structure) and $R\bar{3}m$ AgBiS₂, unless otherwise stated, having been demonstrated to

accurately predict the electronic structures of semiconductor materials^{59,60}. To account for relativistic effects, due to the presence of heavy-atom elements Ag and Bi, spin–orbit coupling effects were included in all electronic and optical calculations (HSE06+SOC).

Secondly, to investigate the effects of both partial order and inhomogeneous disorder (i.e. cation segregation with Ag-rich and Bi-rich regions) on the cation sublattice, all possible configurations for AgBiS₂ in a 32-atom rocksalt structure were enumerated using the Transformer package⁶¹, yielding 440 symmetry-inequivalent arrangements. Here, the PBEsol⁴² semi-local exchange-correlation functional was used for geometry optimisations and energetic analysis, motivated by its well-established accuracy for the structural relaxation of bulk solids⁴³ and moderate computational cost. Moreover, this functional was tested against both experiment and the computationally-intensive HSE06 hybrid DFT functional for bulk geometry optimisation and energetics respectively, using all known structures in the Ag-Bi-S system. Here, PBEsol was found to accurately reproduce experimentally-reported crystal structures, with a mean absolute error <1.5% in the lattice parameters, as well as reproducing the energetic ordering of phases on the convex hull according to both HSE06 and experiment.

To ensure consistency when comparing the results of these calculations to that of $Fm\bar{3}m$ (SQS) AgBiS₂, a new 32-atom SQS supercell was generated using the same procedure as outlined above, and relaxed with PBEsol. In this case, a perfect ‘objective function’ match to the true disordered solution was obtained. While appropriate for structural and energetic analysis of cation configurations in AgBiS₂, semi-local DFT is known to severely underestimate electronic bandgaps^{64,65}, and so the HSE06+SOC hybrid DFT functional was used to calculate the optical and electronic properties of these configurations. In this case, downsampling of the Fock exchange matrix by a factor of 2 (NKRED = 2) was employed to reduce the computational cost to a manageable level. This choice was confirmed to affect the electronic bandgap by <0.05 eV for the 32-atom SQS supercell.

To investigate the impact of supercell size on the calculated properties, the 32-atom SQS supercell was also relaxed with the HSE06 functional, to then compare with the 64-atom structure. The total energy was found to match that of the 64-atom SQS supercell to <1 meV/atom, while the bandgap was found to increase slightly from 0.69 eV to 0.83 eV for the 32-atom supercell.

Post-processing. Primitive and unfolded electronic band structure diagrams were generated using sumo and PyVaspWfc^{46,47} respectively. Effmass was used to calculate carrier effective masses⁶⁸, and photoemission spectra were generated using Galore⁶⁹. COHP analysis and charge-density partitioning was performed using LOBSTER,⁵⁰ and the vasp package⁵¹ was used to calculate radial distribution functions. The pymatgen package was used throughout for manipulation and analysis of calculation inputs and outputs⁷².

Chemicals and materials. Reagents were purchased from Sigma Aldrich, except SnO₂ colloid precursor (tin (IV) oxide, 15% in H₂O colloidal dispersion), which was obtained from Alfa Aesar. Poly (triaryl amine) (PTAA) was purchased from EM index and Poly [[4,8-bis[(2-ethylhexyl)oxy]benzo[1,2-b:4,5-b']dithiophene-2,6-diyl][3-fluoro-2-[(2-ethylhexyl) carbonyl]thieno [3,4-b]thiophenediyl]] (PTB7) was purchased from 1-materials.

Synthesis of AgBiS₂ nanocrystals. The Schlenk technique was used to synthesize AgBiS₂ nanocrystals, following previous report with modifications^{1,14}. 4 mmol Bi(OAc)₃, 3.2 mmol Ag(OAc), 24 mL oleic acid (OA) and 15 mL 1-octadecene (ODE) was pumped at 100°C for 2 hours (~0.2 mbar) to remove oxygen and moisture. 4 mmol hexamethyldisilathiane (HMS) dissolved in 5 mL ODE was quickly injected into the flask. The heating mantle was removed and the reaction was cooled down with water bath for ~5 min. After that, the crude solution was left stirring for 1 hour at room temperature. The nanocrystals were isolated by adding acetone, followed by centrifugation. The extracted nanocrystals were re-dispersed in toluene and acetone was added to precipitate nanocrystals. The re-dispersion/precipitation was

repeated once more. Finally, the obtained AgBiS₂ nanocrystals powder was dispersed in anhydrous toluene (20 mg mL⁻¹) and stored in ambient atmosphere for device fabrication.

Characterization of AgBiS₂ nanocrystals and films. Films exchanged with 3-mercaptopropionic acid (3-MPA) were grown on glass substrates, followed by annealing at different temperatures in glovebox. The thicknesses were measured using a profilometer. The complex refractive index was measured at various angles using broadband Sopra Ellipsometer GES5E. The software SEMILAB Spectroscopic Ellipsometry Analyzer was utilized to fit a model of stacked layers of appropriate optical constants and the thickness from profilometer was used as an input. The absorption coefficients are calculated from extinction coefficients. XRD data were collected using a Rigaku Smartlab powder diffractometer in Bragg-Brentano geometry with Cu K α radiation. XPS measurements was performed with a SPECS PHOIBOS 150 hemispherical analyser (SPECS GmbH, Berlin, Germany) in ultra-high vacuum conditions (10⁻¹⁰ mbar), with a monochromatic K α x-ray source (1486.74 eV) at the Institut Catala de Nanociencia i Nanotecnologia (ICN2). TEM was performed at the Scientific and Technological Centres of the University of Barcelona (CCiT-UB). TEM images were obtained using a JEOL 2100 microscope operating at an accelerating voltage of 200 kV.

Optical modelling and Spectroscopic limited maximum efficiency. A homemade MATLAB code was used to implement the transfer matrix formalism. We assumed that each layer was flat and considered no scattering effects. Short circuit current density was calculated with the assumption of 100% internal quantum efficiency. Spectroscopic Limited Maximum Efficiency (SLME) was calculated according to:

$$SLME = P_{max}$$

$$P = -V * \left\{ J_0 \left[\exp \left(\frac{eV}{kT} \right) - 1 \right] - J_{sc,TMM} \right\}$$

where e the elementary charge, k the Boltzmann constant, T the temperature, and J_0 the dark saturation current density, calculated with the assumption of only radiative recombination:

$$J_0 = e * \int_0^{+\infty} EQE_{TMM} * \phi_{BB}(E) dE$$

where EQE_{TMM} is the calculated total absorption in $AgBiS_2$ NCs layer, and ϕ_{BB} is the black body radiation spectra at 300 K.

Solar cell fabrication. All solar cell fabrication steps were performed in ambient air, unless with specific descriptions. ITO covered glass substrates (Universität Stuttgart, Institut für Großflächige Mikroelektronik) were cleaned by ultra sonication in soapy water, acetone and isopropanol for 20 min each and dried with nitrogen, followed with 0.5 h UV/Ozone treatment. SnO_2 electron transport layer was then spin cast from diluted Alfa SnO_2 colloid solution (1:5.6 v/v with H_2O) with spin speed of 2000 rpm and annealed at $270^\circ C$ for 15 min. Afterwards, three layers of $AgBiS_2$ nanocrystals were deposited from 20 mg mL^{-1} toluene solution via layer-by-layer (LbL) method. For each $AgBiS_2$ nanocrystals layer, one drop of $AgBiS_2$ NCs solution was spin-coated onto SnO_2 /ITO substrates during spinning (2000 rpm). 3-Mercaptopropionic acid (MPA)/methanol (1% v/v) solution was then applied to the nanocrystals film for 45s, followed by two rinse-spin steps with methanol and once with toluene. The films were transferred into glovebox for 10 min annealing at $115^\circ C$ and then stored in dry air before spin-coating PTB7 (5 mg mL^{-1} in dichlorobenzene) or PTAA solution (2 mg mL^{-1} in toluene) at 3000 rpm. Finally, a Kurt J. Lesker Nano36 system was used to deposit 3 nm of MoO_3 and 120 nm of Ag through a shadow mask to produce solar cells with a diameter of 2 mm (area of 3.14 mm^2).

Solar cell characterization. All device characterization was performed in air under ambient conditions. Current-voltage measurements were performed with a Keithley 2400 Sourcemeter

and a Newport Oriel Sol3A solar simulator with an AM1.5G filter. The intensity of the solar light was calibrated using a Hamamatsu S1336 silicon photodiode that had been calibrated at the Fraunhofer Institute of Solar Energy Systems, Freiburg, Germany. The solar cells were measured with and without masks, and slightly lower V_{oc} was observed when measuring with masks, due to masking effect. For certified cells, appropriate masks have always been used. The EQE was measured using a Newport Cornerstone 260 monochromator, a Thorlabs MC2000 chopper, a Stanford Research SR570 trans-impedance amplifier and a Stanford Research SR830 lock-in amplifier. A calibrated Newport 818-UV photodetector was used as a reference. Shelf stability was obtained from devices stored in air without encapsulation. For the maximum power point (MPP) measurement, the MPP voltage ($t = 0$) was measured before MPP testing. The device was then held at the MPP voltage ($t = 0$) for operating stability test. The device was unencapsulated under AM1.5G illumination. All devices were characterized under ambient condition with relative humidity $> 60\%$ and ambient temperature $\sim 25^\circ\text{C}$. Longer time photo-stability was measured with a low-cost solar simulator from ABET technologies. Transient photocurrent and photovoltage of the devices were measured with an in-house-built set-up. The set-up comprises a LED lamp to provide steady state white light bias, a 637nm laser and an Agilent 4000X oscilloscope. The V_{oc} of devices are controlled by the light intensity of the LED lamp and the transient voltage induced by laser pulse are controlled within 5% of the V_{oc} . Time-of-flight method is used for the mobility measurements. Electron only and hole only devices are fabricated with the structure of ITO/SnO₂/AgBiS₂/PCBM/Ag and ITO/NiO_x/AgBiS₂/PTAA/MoO_x/Ag. The thickness of AgBiS₂ layer was controlled to ~ 200 nm. A 520 nm nanosecond laser was used as the excitation light. Photocurrent decay was recorded at various bias with an oscilloscope. The mobility was calculated by fitting the $d^2/t-V_{bias}$ plots.

Acknowledgements

The authors acknowledge financial support from the European Research Council (ERC) under the European Union's Horizon 2020 research and innovation programme (grant agreement no. 725165) and the Fundació Joan Ribas Araquistain (FJRA). This project was supported also by Fundació Privada Cellex, the program CERCA, EQC2019-005797-P (AEI/FEDER UE), 2017SGR1373 and "Severo ochoa" Center of Excellence CEX2019-000910-S – Funded by the Spanish State Research Agency. I. Burgués-Ceballos acknowledges support from the Government of Catalonia's Beatriu de Pinós postdoctoral programme (grant number 2017BP00241). This project has received funding from the European Union's Horizon 2020 research and innovation programme under the Marie Skłodowska-Curie grant agreement No. 754558. Seán R. Kavanagh thanks Liam Harnett-Caulfield for help with using the ATAT software package, Dr. Yong-Seok Choi for help with calculating the Madelung potentials and acknowledges the EPSRC Centre for Doctoral Training in the Advanced Characterisation of Materials (CDT-ACM)(EP/S023259/1) for funding a PhD studentship. We acknowledge the use of the UCL Kathleen High Performance Computing Facility (Kathleen@UCL), the Imperial College Research Computing Service, and associated support services, in the completion of this work. Via membership of the UK's HEC Materials Chemistry Consortium, which is funded by the EPSRC (EP/L000202, EP/R029431, EP/T022213), this work used the ARCHER2 UK National Supercomputing Service and the UK Materials and Molecular Modelling (MMM) Hub (Thomas – EP/P020194 & Young – EP/T022213). DOS acknowledges support from the EPSRC (EP/N01572X/1) and from the European Research Council, ERC (Grant No. 758345).

Author contributions

G.K. supervised and directed the study. Y.W. and G.K. conceived the idea, designed this study and co-wrote the manuscript with feedback from co-authors. Y.W. synthesized the AgBiS₂

NCs, performed material characterization, fabricated, characterized the solar cells, and analysed the data, with the help of I.B. Y.W. did the optical modelling. S.K. designed and conducted the theoretical modelling, analysed the DFT simulations, interpreted the data, provided insights and contributed to manuscript writing. D.O.S and A.W. supervised the theoretical modelling.

Additional information

Supplementary information is available in the online version of the paper. Correspondence and request materials should be addressed to G.K.

Data and code availability

The data and code that supported the current study are available from the corresponding author on request.

Competing financial interests

The authors declare no competing financial interests.

References

1. Bernechea, M. *et al.* Solution-processed solar cells based on environmentally friendly AgBiS₂ nanocrystals. *Nat. Photonics* **10**, 521–525 (2016).
2. Boles, M. A., Ling, D., Hyeon, T. & Talapin, D. V. The surface science of nanocrystals. *Nat. Mater.* **15**, 364–364 (2016).
3. Green, M. A. & Bremner, S. P. Energy conversion approaches and materials for high-efficiency photovoltaics. *Nat. Mater.* **16**, 23–34 (2017).
4. Massiot, I., Cattoni, A. & Collin, S. Progress and prospects for ultrathin solar cells. *Nat. Energy* **5**, 959–972 (2020).
5. Chen, H.-L. *et al.* A 19.9%-efficient ultrathin solar cell based on a 205-nm-thick GaAs absorber and a silver nanostructured back mirror. *Nat. Energy* **4**, 761–767 (2019).

- 1 6. Adhyaksa, G. W. P., Johlin, E. & Garnett, E. C. Nanoscale Back Contact Perovskite Solar Cell
2 Design for Improved Tandem Efficiency. *Nano Lett.* **17**, 5206–5212 (2017).
- 3 7. Bosson, C. J. *et al.* Cation disorder and phase transitions in the structurally complex solar cell
4 material Cu₂ZnSnS₄. *J. Mater. Chem. A* **5**, 16672–16680 (2017).
- 5 8. Chen, W., Dahliah, D., Rignanese, G.-M. & Hautier, G. Origin of the low conversion efficiency
6 in Cu₂ZnSnS₄ kesterite solar cells: the actual role of cation disorder. *Energy Environ. Sci.* **14**, 3567–
7 3578 (2021).
- 8 9. Malerba, C., Valentini, M. & Mittiga, A. Cation Disorder In Cu₂ZnSnS₄ Thin Films: Effect On
9 Solar Cell Performances. *Sol. RRL* **1**, 1700101 (2017).
- 10 10. Li, J. *et al.* Defect Control for 12.5% Efficiency Cu₂ZnSnSe₄ Kesterite Thin-Film Solar Cells by
11 Engineering of Local Chemical Environment. *Adv. Mater.* **n/a**, 2005268.
- 12 11. Zawadzki, P., Zakutayev, A. & Lany, S. Entropy-Driven Clustering in Tetrahedrally Bonded
13 Multinary Materials. *Phys. Rev. Appl.* **3**, (2015).
- 14 12. Mohan, R. Green bismuth. *Nat. Chem.* **2**, 336–336 (2010).
- 15 13. Vesborg, P. C. K. & Jaramillo, T. F. Addressing the terawatt challenge: scalability in the supply
16 of chemical elements for renewable energy. *RSC Adv.* **2**, 7933 (2012).
- 17 14. Burgués-Ceballos, I., Wang, Y., Akgul, M. Z. & Konstantatos, G. Colloidal AgBiS₂ nanocrystals
18 with reduced recombination yield 6.4% power conversion efficiency in solution-processed solar cells.
19 *Nano Energy* **75**, 104961 (2020).
- 20 15. Kopula Kesavan, J. *et al.* Cation Disorder and Local Structural Distortions in Ag_xBi_{1-x}S₂
21 Nanoparticles. *Nanomaterials* **10**, 316 (2020).
- 22 16. Schnepf, R. R. *et al.* Utilizing Site Disorder in the Development of New Energy-Relevant
23 Semiconductors. *ACS Energy Lett.* **5**, 2027–2041 (2020).
- 24 17. Yang, W.-C., Miskin, C. K., Carter, N. J., Agrawal, R. & Stach, E. A. Compositional
25 Inhomogeneity of Multinary Semiconductor Nanoparticles: A Case Study of Cu₂ZnSnS₄. *Chem.*
26 *Mater.* **26**, 6955–6962 (2014).
- 27 18. Hao, M. *et al.* Ligand-assisted cation-exchange engineering for high-efficiency colloidal
28 Cs_{1-x}Fa_xPbI₃ quantum dot solar cells with reduced phase segregation. *Nat. Energy* **5**, 79–88 (2020).
- 29 19. Ju, M.-G., Dai, J., Ma, L., Zhou, Y. & Zeng, X. C. AgBiS₂ as a low-cost and eco-friendly all-
30 inorganic photovoltaic material: nanoscale morphology–property relationship. *Nanoscale Adv.* **2**,
31 770–776 (2020).
- 32 20. Viñes, F., Bernechea, M., Konstantatos, G. & Illas, F. Matildite versus schapbachite: First-
33 principles investigation of the origin of photoactivity in AgBiS₂. *Phys. Rev. B* **94**, 235203 (2016).
- 34 21. Guin, S. N., Banerjee, S., Sanyal, D., Pati, S. K. & Biswas, K. Origin of the Order–Disorder
35 Transition and the Associated Anomalous Change of Thermopower in AgBiS₂ Nanocrystals: A
36 Combined Experimental and Theoretical Study. *Inorg. Chem.* **55**, 6323–6331 (2016).
- 37 22. Khan, M. D. *et al.* Electrochemical investigation of uncapped AgBiS₂ (schapbachite)
38 synthesized using *in situ* melts of xanthate precursors. *Dalton Trans.* **48**, 3714–3722 (2019).

23. Ren, X. *et al.* *In situ* exsolution of Ag from AgBiS₂ nanocrystal anode boosting high-performance potassium-ion batteries. *J. Mater. Chem. A* **8**, 15058–15065 (2020).
24. Liu, M. *et al.* Hybrid organic–inorganic inks flatten the energy landscape in colloidal quantum dot solids. *Nat. Mater.* **16**, 258–263 (2017).
25. Kagan, C. R. & Murray, C. B. Charge transport in strongly coupled quantum dot solids. *Nat. Nanotechnol.* **10**, 1013–1026 (2015).
26. Wong, J., Omelchenko, S. T. & Atwater, H. A. Impact of Semiconductor Band Tails and Band Filling on Photovoltaic Efficiency Limits. *ACS Energy Lett.* **6**, 52–57 (2021).
27. Treharne, R. E. *et al.* Optical Design and Fabrication of Fully Sputtered CdTe/CdS Solar Cells. *J. Phys. Conf. Ser.* **286**, 012038 (2011).
28. ElAnzeery, H. *et al.* Refractive index extraction and thickness optimization of Cu₂ZnSnSe₄ thin film solar cells. *Phys. Status Solidi A* **212**, 1984–1990 (2015).
29. *Handbook of optical constants of solids*. (Academic Press, 1998).
30. Manzoor, S. *et al.* Optical modeling of wide-bandgap perovskite and perovskite/silicon tandem solar cells using complex refractive indices for arbitrary-bandgap perovskite absorbers. *Opt. Express* **26**, 27441 (2018).
31. Chen, C. *et al.* Characterization of basic physical properties of Sb₂Se₃ and its relevance for photovoltaics. *Front. Optoelectron.* **10**, 18–30 (2017).
32. Pettersson, L. A. A., Roman, L. S. & Inganäs, O. Modeling photocurrent action spectra of photovoltaic devices based on organic thin films. *J. Appl. Phys.* **86**, 487–496 (1999).
33. Centurioni, E. Generalized matrix method for calculation of internal light energy flux in mixed coherent and incoherent multilayers. *Appl. Opt.* **44**, 7532 (2005).
34. Guillemoles, J.-F., Kirchartz, T., Cahen, D. & Rau, U. Guide for the perplexed to the Shockley–Queisser model for solar cells. *Nat. Photonics* **13**, 501–505 (2019).
35. Gilmore, R. H. *et al.* Epitaxial Dimers and Auger-Assisted Detrapping in PbS Quantum Dot Solids. *Matter* **1**, 250–265 (2019).
36. Bagus, P. S., Illas, F., Pacchioni, G. & Parmigiani, F. Mechanisms responsible for chemical shifts of core-level binding energies and their relationship to chemical bonding. *J. Electron Spectrosc. Relat. Phenom.* **100**, 215–236 (1999).
37. Tambo, T. & Tatsuyama, C. XPS Study on the Chemical Shifts of Crystalline III–VI Layered Compounds. *J. Phys. Soc. Jpn.* **54**, 4382–4389 (1985).
38. Akgul, M. Z., Figueroba, A., Pradhan, S., Bi, Y. & Konstantatos, G. Low-Cost RoHS Compliant Solution Processed Photovoltaics Enabled by Ambient Condition Synthesis of AgBiS₂ Nanocrystals. *ACS Photonics* **7**, 588–595 (2020).
39. Hu, L. *et al.* Enhanced optoelectronic performance in AgBiS₂ nanocrystals obtained via an improved amine-based synthesis route. *J. Mater. Chem. C* **6**, 731–737 (2018).
40. Oh, J. T. *et al.* Water-resistant AgBiS₂ colloidal nanocrystal solids for eco-friendly thin film photovoltaics. *Nanoscale* **11**, 9633–9640 (2019).

- 1 41. Pan, H. *et al.* Advances in design engineering and merits of electron transporting layers in
2 perovskite solar cells. *Mater. Horiz.* 10.1039/D0MH00586J (2020) doi:10.1039/D0MH00586J.
- 3 42. Diedenhofen, S. L., Bernechea, M., Felter, K. M., Grozema, F. C. & Siebbeles, L. D. A. Charge
4 Photogeneration and Transport in AgBiS₂ Nanocrystal Films for Photovoltaics. *Sol. RRL* **3**, 1900075
5 (2019).
- 6 43. Cao, Y., Stavrinadis, A., Lasanta, T., So, D. & Konstantatos, G. The role of surface passivation
7 for efficient and photostable PbS quantum dot solar cells. *Nat. Energy* **1**, 16035 (2016).
- 8 44. Irfan *et al.* Energy level evolution of air and oxygen exposed molybdenum trioxide films.
9 *Appl. Phys. Lett.* **96**, 243307 (2010).
- 10 45. Yu, B.-B. *et al.* Heterogeneous 2D/3D Tin-Halides Perovskite Solar Cells with Certified
11 Conversion Efficiency Breaking 14%. *Adv. Mater.* 2102055 (2021) doi:10.1002/adma.202102055.
- 12 46. Jiang, X. Ultra-high open-circuit voltage of tin perovskite solar cells via an electron
13 transporting layer design. *Nat. Commun.* **7** (2020).
- 14 47. Choi, Y. C., Lee, D. U., Noh, J. H., Kim, E. K. & Seok, S. I. Highly Improved Sb₂S₃ Sensitized-
15 Inorganic–Organic Heterojunction Solar Cells and Quantification of Traps by Deep-Level Transient
16 Spectroscopy. *Adv. Funct. Mater.* **24**, 3587–3592 (2014).
- 17 48. Wu, C. *et al.* Water Additive Enhanced Solution Processing of Alloy Sb₂(S_{1-x}Se_x)₃-Based
18 Solar Cells. *Sol. RRL* **4**, 1900582 (2020).
- 19 49. Huber, S. P. *et al.* AiiDA 1.0, a scalable computational infrastructure for automated
20 reproducible workflows and data provenance. *Sci. Data* **7**, 300 (2020).
- 21 50. Kresse, G. & Hafner, J. Ab initio molecular dynamics for liquid metals. *Phys. Rev. B* **47**, 558–
22 561 (1993).
- 23 51. Kresse, G. & Furthmüller, J. Efficiency of ab-initio total energy calculations for metals and
24 semiconductors using a plane-wave basis set. *Comput. Mater. Sci.* **6**, 15–50 (1996).
- 25 52. Kresse, G. & Furthmüller, J. Efficient iterative schemes for ab initio total-energy calculations
26 using a plane-wave basis set. *Phys. Rev. B - Condens. Matter Mater. Phys.* **54**, 11169–11186 (1996).
- 27 53. Blöchl, P. E. Projector augmented-wave method. *Phys. Rev. B* **50**, 17953–17979 (1994).
- 28 54. Zunger, A., Wei, S.-H., Ferreira, L. G. & Bernard, J. E. Special quasirandom structures. *Phys.*
29 *Rev. Lett.* **65**, 353–356 (1990).
- 30 55. van de Walle, A., Asta, M. & Ceder, G. The alloy theoretic automated toolkit: A user guide.
31 *Calphad* **26**, 539–553 (2002).
- 32 56. van de Walle, A. *et al.* Efficient stochastic generation of special quasirandom structures.
33 *Calphad* **42**, 13–18 (2013).
- 34 57. Geller, S. & Wernick, J. H. Ternary semiconducting compounds with sodium chloride-like
35 structure: AgSbSe₂, AgSbTe₂, AgBiS₂, AgBiSe₂. *Acta Crystallogr.* **12**, 46–54 (1959).
- 36 58. Heyd, J., Scuseria, G. E. & Ernzerhof, M. Hybrid functionals based on a screened Coulomb
37 potential. *J. Chem. Phys.* **118**, 8207–8215 (2003).

59. Borlido, P. *et al.* Exchange-correlation functionals for band gaps of solids: benchmark, reparametrization and machine learning. *Npj Comput. Mater.* **6**, 96 (2020).
60. Krukau, A. V., Vydrov, O. A., Izmaylov, A. F. & Scuseria, G. E. Influence of the exchange screening parameter on the performance of screened hybrid functionals. *J. Chem. Phys.* **125**, 224106 (2006).
61. Skelton, J. *JMSkelton/Transformer*. (2021).
62. Perdew, J. P. *et al.* Restoring the Density-Gradient Expansion for Exchange in Solids and Surfaces. *Phys. Rev. Lett.* **100**, 136406 (2008).
63. Csonka, G. I. *et al.* Assessing the performance of recent density functionals for bulk solids. *Phys. Rev. B* **79**, 155107 (2009).
64. Hoyer, R. L. Z. *et al.* Perovskite-Inspired Photovoltaic Materials: Toward Best Practices in Materials Characterization and Calculations. *Chem. Mater.* **29**, 1964–1988 (2017).
65. Huang, Y.-T., Kavanagh, S. R., Scanlon, D. O., Walsh, A. & Hoyer, R. L. Z. Perovskite-inspired materials for photovoltaics and beyond—from design to devices. *Nanotechnology* **32**, 132004 (2021).
66. Zheng, Q. *QijingZheng/VaspBandUnfolding*. (2021).
67. Popescu, V. & Zunger, A. Extracting E versus $k \rightarrow$ effective band structure from supercell calculations on alloys and impurities. *Phys. Rev. B* **85**, 085201 (2012).
68. D. Whalley, L. effmass: An effective mass package. *J. Open Source Softw.* **3**, 797 (2018).
69. J Jackson, A., M Ganose, A., Regoutz, A., G. Egdell, R. & O Scanlon, D. Galore: Broadening and weighting for simulation of photoelectron spectroscopy. *J. Open Source Softw.* **3**, 773 (2018).
70. Nelson, R. *et al.* LOBSTER: Local orbital projections, atomic charges, and chemical-bonding analysis from projector-augmented-wave-based density-functional theory. *J. Comput. Chem.* **41**, 1931–1940 (2020).
71. Morgan, B. J. *vasppy*. zenodo.org/record/4460130 (2021) doi:10.5281/zenodo.4460130.
72. Ong, S. P. *et al.* Python Materials Genomics (pymatgen): A robust, open-source python library for materials analysis. *Comput. Mater. Sci.* **68**, 314–319 (2013).

FIGURES

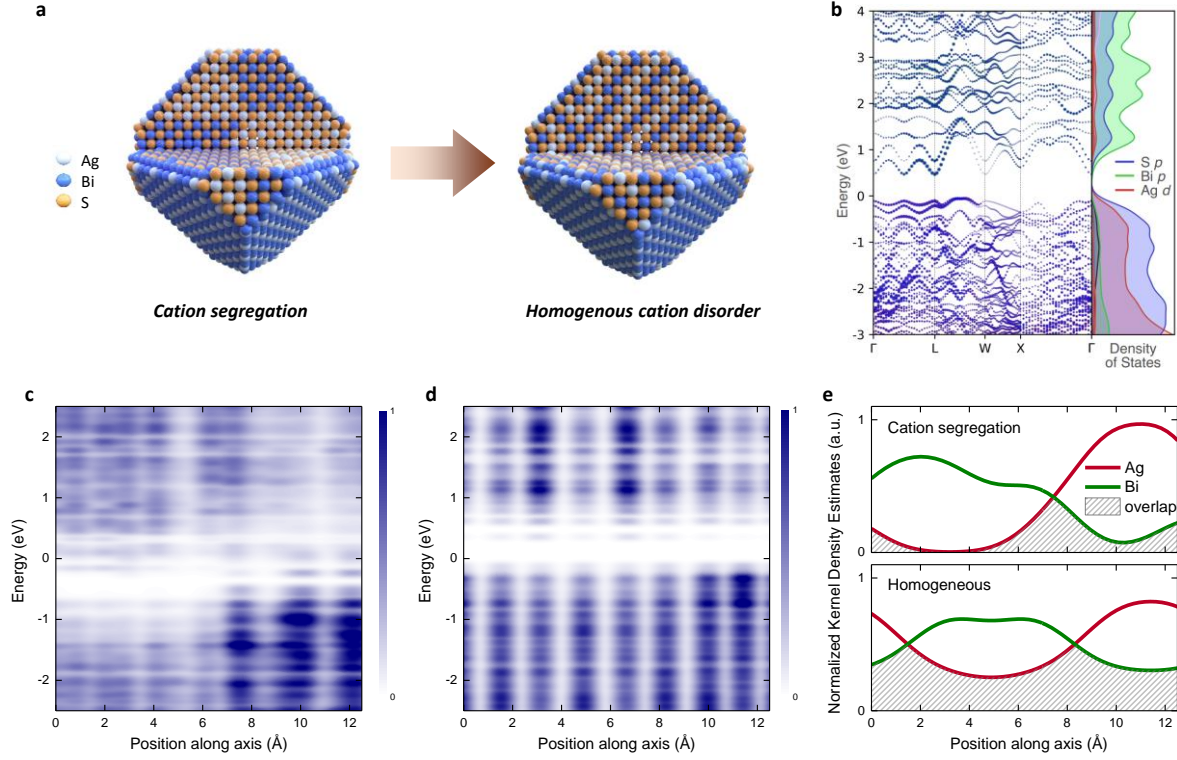


Figure 1. Absorption enhancement via cation disorder homogenisation. **a**, Schematic of AgBiS₂ NCs with cation segregation and homogeneous cation disorder. **b**, Effective electronic band structure of homogeneous disordered AgBiS₂, alongside the electronic density of states. Atomic orbital contributions have been projected with the colour map (S *p*: blue, Bi *p*: green, Ag *d*: red). VBM set to 0 eV. **c**, Planar-averaged local electronic density of states (LDOS) for cation segregated AgBiS₂. **d**, Planar-averaged local electronic density of states for homogeneous cation disordered AgBiS₂. **e**, Normalized Kernel density estimates (KDEs) of Ag and Bi for cation segregation and homogeneous cation disordered AgBiS₂. Shadow area shows the overlap of Ag and Bi KDEs.

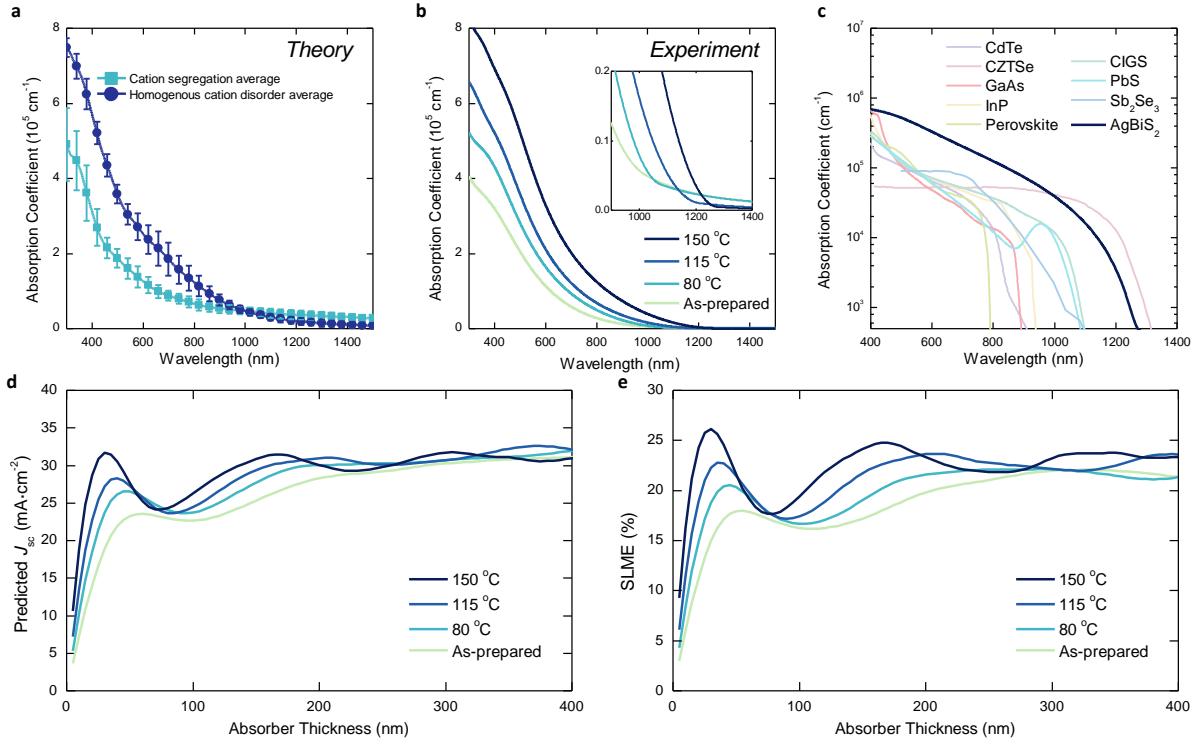


Figure 2. Absorption coefficients and optical modelling. **a**, Simulated absorption coefficients of AgBiS₂ with different cation distributions. Error bars indicate the standard deviation. **b**, Absorption coefficients of AgBiS₂ NCs annealed at different temperatures. Inset: Zoom-in of long wavelength region. **c**, Absorption coefficient of AgBiS₂ NCs films compared with other photovoltaic materials (CdTe²⁷, CZTSe²⁸, GaAs⁴, InP²⁹, Perovskite³⁰, CIGS⁴, PbS, Sb₂Se₃³¹). **d**, Predicted short circuit current density (J_{sc}) of AgBiS₂ NCs using the transfer matrix method (TMM). **e**, Spectroscopic Limited Maximum Efficiency (SLME) of AgBiS₂ NCs as a function of film thickness.

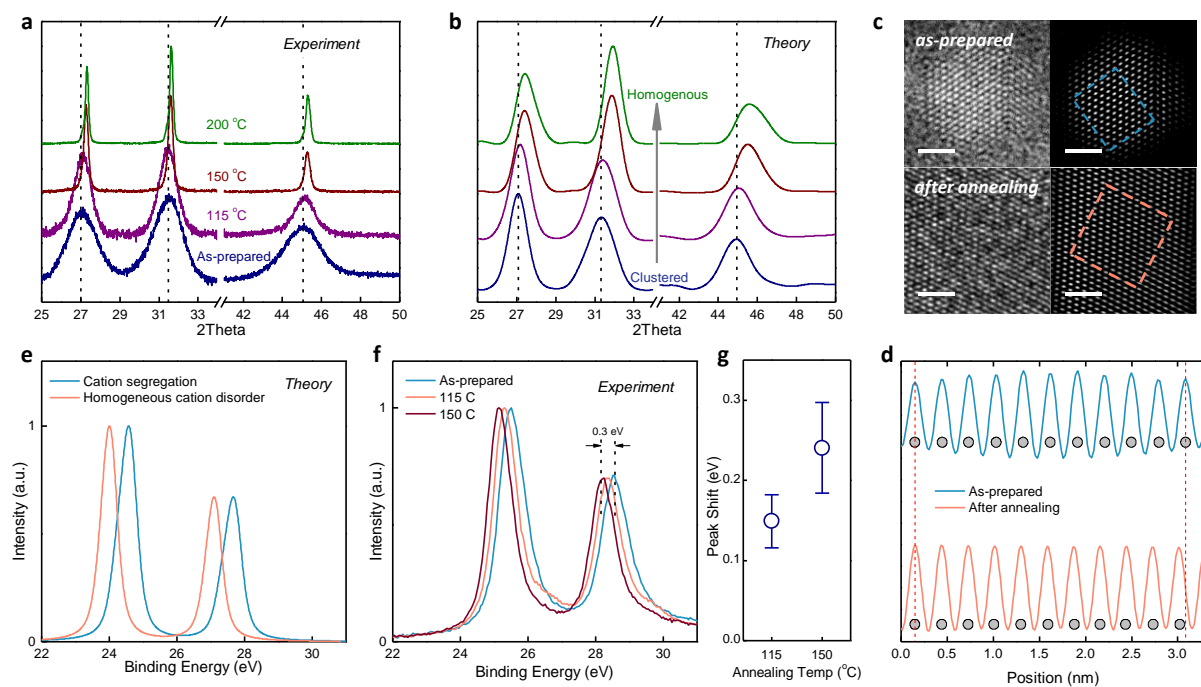


Figure 3. Characterization of cation configuration transition. (Clockwise) a, Experimental XRD patterns of AgBiS₂ NCs annealed at different temperatures. **b**, Simulated XRD of 10nm AgBiS₂ NCs with varying cation distribution homogeneity, from cation segregation to homogeneous cation disorder. **c**, High resolution transmission electron microscope (HRTEM) images of AgBiS₂ NCs before and after 200 °C annealing. Scale bar: 2 nm. **d**, Integrated line profiles of the {200} crystal plane indicated by dashed lines in **c**. **e**, Simulated valence band x-ray photoelectron (XPS) spectra of AgBiS₂ with different cation configurations. **f**, Experimental XPS spectra of AgBiS₂ NCs annealed at different temperatures. Dashed lines indicates the peak positions before and after annealing. **g**, Statistics of XPS peak shifts from three different batches of samples. Error bars indicate the standard deviation.

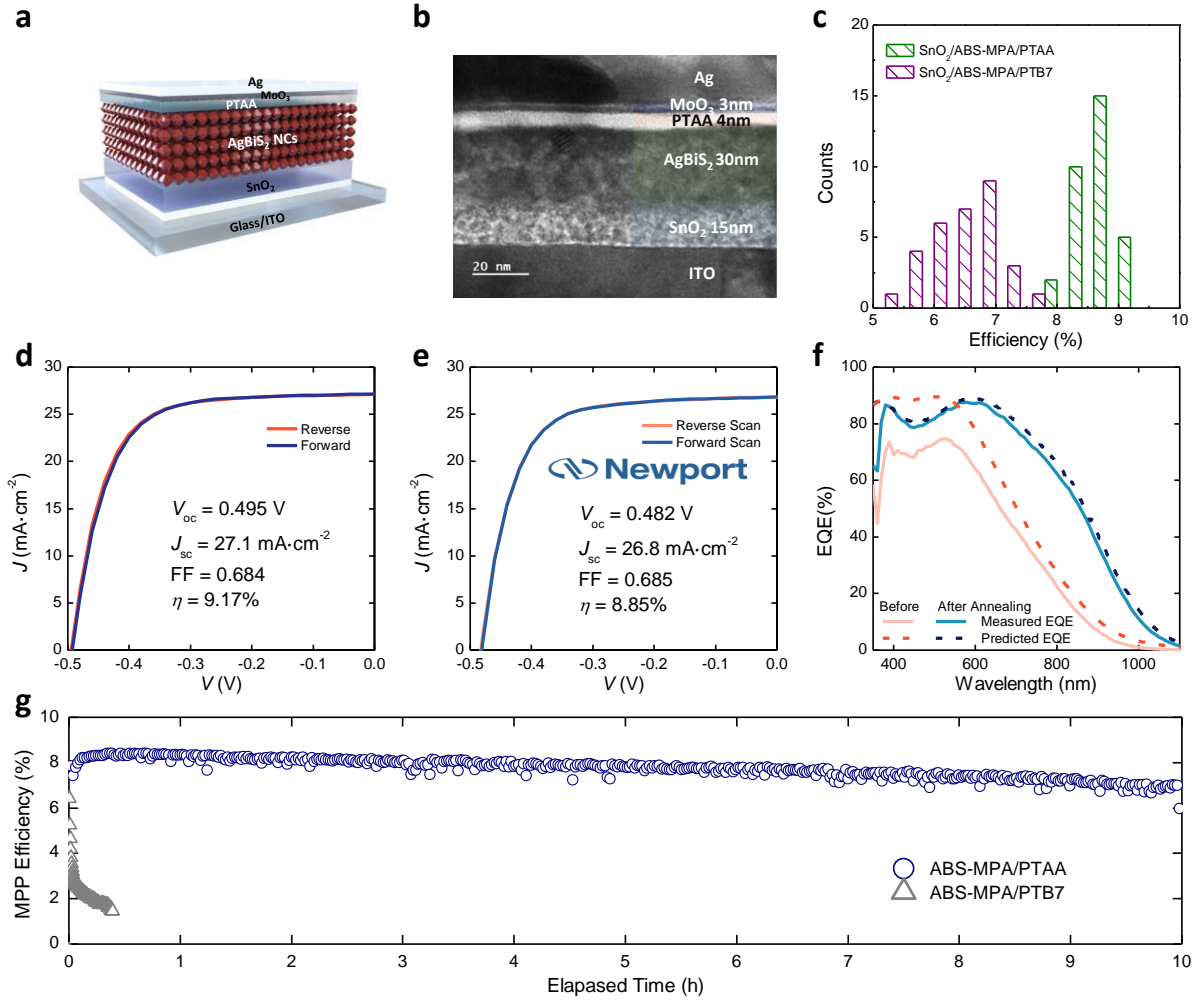


Figure 4. Ultrathin AgBiS₂ NCs solar cells. **a**, Schematic of the AgBiS₂ NCs solar cells. **b**, Cross-sectional TEM image of the device. **c**, Statistical histogram of AgBiS₂ NCs solar cells with PTB7 and PTAA as hole transport layer (HTL). **d**, *J*-*V* curves of the champion device with PTAA as HTL. **e**, *J*-*V* curves of AgBiS₂ NCs solar cells certified at Newport, USA. **f**, Measured and predicted EQE curves of devices before and after annealing. **g**, Maximum power point (MPP) test of AgBiS₂ devices with PTB7 and PTAA as HTLs.

TABLES

Table 1 Photovoltaic parameters of devices based on different hole transport layers

	V_{oc} (V)	J_{sc} (mA·cm ⁻²)	FF	PCE (%)
AgBiS ₂ NCs/PTB7	0.437 ± 0.011	25.59 ± 0.81	0.57 ± 0.03	6.42 ± 0.55
Champion device	0.450	26.75	0.63	7.63
AgBiS ₂ NCs/PTAA	0.489 ± 0.005	26.99 ± 0.76	0.66 ± 0.02	8.70 ± 0.31
Champion device	0.495	27.11	0.68	9.17
Certified	0.482	26.8	0.68	8.85

Note: statistics are based on 31 different devices.